JOURNAL OF SPACECRAFT AND ROCKETS
Vol. 45, No. 6, November–December 2008

Surface Direct Current Discharge for Hypersonic Flow Control

J. S. Shang*
Wright State University, Dayton, Ohio 45435

DOI: 10.2514/1.37009

A hypersonic flow control mechanism has been found by using a near-surface gas discharge as a small flow perturbation and amplifying it by viscous–inviscid interaction. Substantiated evidence was collected from a plasma channel that operated at a hypersonic Mach number of 5.15. This flow control mechanism is simulated by integrating a drift-diffusion weakly ionized air model with compressible Navier–Stokes equations. The side-by-side investigations were performed for flows over surface plasma generated by a pair of embedded electrodes on a sharp leading wedge and on the entrance surface of rectangular and cylindrical constant cross section inlet models. The present effort demonstrates that the effect of a direct current discharge, when amplified by the viscous–inviscid interaction, can become a mechanism for hypersonic flow control. The research results from computational simulations, after being verified with experimental observations, are summarized for a virtual hypersonic leading-edge strake and virtual variable-area hypersonic inlet cowl.

Nomenclature

$\mathbf{B}$	=	magnetic field strength
D_e, D_+	=	diffusion coefficients of electron and ion, respectively
$\mathbf{E}$	=	electric field strength
e	=	specific internal energy
$\mathbf{F}$	=	flux vector of conservation equations
$\mathbf{i}$, $\mathbf{j}$	=	unit vector of x, y coordinates
$\mathbf{J}$	=	electric current density
n_e, n_+	=	number density of electron and ion, respectively
$\mathbf{q}$	=	conductive heat transfer
U	=	dependent variables of conservation equations
$\mathbf{u}$	=	velocity vector, $\mathbf{u}(u, v)$
Γ_e, Γ_+	=	electron and ion number density flux vector
γ	=	secondary emission coefficient
ε	=	electric permittivity
μ	=	molecular viscosity
μ_e, μ_+	=	electron and ion mobility, respectively
μ_m	=	magnetic permeability
ρ	=	density
σ	=	electric conductivity
τ	=	shear stress tensor
φ	=	electric potential
χ	=	viscous–inviscid interaction parameter, $\chi = M^3(C/Re)^{1/2}$

Introduction

DIRECT current discharge (DCD) has been widely adopted as a hypersonic flow control mechanism [1–15]. Some of the early flow control ideas have been introduced since the late 1990s by Bityurin et al. [1,3], Leonov et al. [2], and many others. Macheret et al. have also advocated the idea of using electron beam ionization for the control of hypersonic scramjet inlets [4]. In their approach, a simple model of a beam-generated ionization profile is used to describe the required electric conductivity for the electromagnetic force. On the other hand, a series of side-by-side computational and experimental investigations of the DCD were conducted in a hypersonic magnetohydrodynamics (MHD) flow channel by Menart et al. [5], Shang and Surzhikov [6], Kimmel et al. [7], and Surzhikov and Shang [8]. An externally applied transverse magnetic field has also been implemented to enhance the flow control effectiveness. For computational simulations, a physical-based nonequilibrium, two-temperature, three-component plasma model was developed based on the classic drift-diffusion theory [8]. Meanwhile, DCD applications have been extended to axisymmetric configurations by Borghi et al. [9] and Cristofolini et al. [10].

More recently, the near-surface electric discharge has been applied to boundary-layer control through hydrodynamic instability of the laminar–turbulent transition, flow separation, and shock position modification [11–15]. In most flow control applications, the magnitude of the applied electromagnetic force appears only on the level of a perturbation in comparison with the aerodynamic inertia of high-speed flow. As a consequence, the impact of flow control is relatively limited, and the control effectiveness is restricted to a local domain. Two obvious remedies to increase the electromagnetic force are either applying a strong magnetic field or using a pulsed discharge. The Lorentz acceleration in plasma is well known and its effectiveness for flow control is strongly dependent on the relative orientation of the fluid motion and magnetic field polarity [8,14]. The advantage of a pulsed discharge is easily understood by the huge disparity in characteristic wave speeds of light and sound. A repetitively pulsed discharge can be an efficient and stable ionization source to sustain a higher electric conductivity in a nonequilibrium gas discharge [15]. These discharge enhancements also bring forth an intensive and much more complex magnetofluiddynamic interaction. Therefore, it is important to better understand the mechanisms and special features of the near-surface discharge for flow control.

The possible electromagnetic effects generated by the DCD are the Lorentz acceleration, electrostatic force, and plasma and electrode heating, all of which have an extremely limited magnitude [8,11]. The Lorentz acceleration is significant only in the presence of an externally applied magnetic field and, due to a relative low current density, the magnitude of this force is just a few kilo-Newtons per meters cubed [16,17]. The electrostatic force is mostly detectable in the cathode layer where the substantial space charge separation occurs; its magnitude is often less than 1 $\mathrm{kN/m^3}$, which is weaker than the pulsing force generated by either the radio frequency or dielectric barrier discharge at atmospheric conditions [18,19]. In

Presented as Paper 1352 at the 46th AIAA Aerospace Science Meeting and Exhibit, Reno, NV, 7–10 January 2008; received 5 February 2008; accepted for publication 16 June 2008.

*Research Professor, Mechanical and Materials Engineering Department. Fellow AIAA.

general, the electromagnetic forces are 2 orders of magnitude lower than the aerodynamic inertia of a typical hypersonic flow. In addition, the orientation of the electrostatic force is mostly downward, toward the electrodes. In a thin shear layer, this force cannot be supported by the shear stress and is therefore transmitted directly to the solid surface [17].

The thermal effects of the DCD include plasma and electrode heating. The former consists of mainly Joule and stochastic heating. The latter, however, is nearly negligible in the absence of an oscillating plasma sheath [20]. The Joule heating concentrates within the cathode layer and becomes a rather small spatial heat source to the surrounding airstream. In the electron collision process for plasma generation, the electrode heating becomes an unavoidable consequence. In a laboratory environment, these two heat fluxes have nearly the same order of magnitude but are much smaller than the energy content of the hypersonic flow. This heat flux enters the flowfield by the convective process with a magnitude less than 1 W/cm^2 [5,7], yet experimental and computational investigations have repeatedly demonstrated a significant DCD flow control effectiveness for hypersonic flows [5–8].

This phenomenon can be understood only in the light of the subsequent viscous–inviscid interaction, which is also a unique feature of hypersonic flows [16,17]. In essence, the flow displacement by a thin boundary layer is no longer negligible under the high-speed flow condition. For flow over a blunt body, the viscous–inviscid interaction is characterized by a vorticity interaction. At a sharp leading edge, the pressure interaction dominates. The outward displacement triggers compression waves that coalesce into an oblique shock. The near-surface DCD becomes a driving mechanism to produce a suddenly increased displacement thickness through Lorentz acceleration with an externally applied magnetic field and heat sources in the shear layer and from the electrode surfaces. The injected thermal flux heats the surrounding airstream and lowers the density within the shear layer, leading to a sudden increase in the displacement thickness. This chain of events accentuates the pressure interaction for which the induced pressure has been successfully formulated and verified with experiments by a single classic interaction parameter, $\chi = M^3(C/Re)^{1/2}$ [21]. This interaction phenomenon actually forms a closed feedback loop between the growth rate of the displacement thickness and the induced streamwise pressure gradient. At the lower χ value, the grow rate is unaltered from the laminar flow ($\delta^* \sim x^{1/2}$), but it changes to a three-quarter power ($\delta^* \sim x^{3/4}$) when the parameter χ exceeds the value of 3. Most importantly, the magnitude of the induced pressure increases according to the cube power of the freestream Mach number. Thus, DCD perturbation can become a viable hypersonic flow control mechanism.

In the present study, the interaction between fluid dynamics and the near-surface DCD is simulated by the magnetofluiddynamic equations with a drift-diffusion weakly ionized gas model. The investigations focus on a glow discharge over the sharp leading edges of a wedge and constant cross-sectional area rectangular and cylindrical inlets. The verified simulated results of the virtual leading-edge strake and virtual variable geometric inlet cowls will be presented.

Governing Equations

In most aerodynamic applications for flow control using plasma actuators, the magnetic Reynolds number, $Re_m = u\sigma\mu_m L$, is often much less than unity [16,17]. According to the investigated flow condition in a hypersonic plasma channel, the Re_m has a value of 8.48×10^{-6}. Under this condition, the induced magnetic field intensity is negligible in comparison with an externally applied field. The magnetofluiddynamic equation at the low magnetic Reynolds number is adopted for the present analysis [22,23]:

$$\partial\rho/\partial t + \nabla\cdot(\rho\mathbf{u}) = 0 \tag{1}$$

$$\partial\rho\mathbf{u}/\partial t + \nabla\cdot(\rho\mathbf{u}\mathbf{u} - \boldsymbol{\tau}) = \mathbf{J}\times\mathbf{B} \tag{2}$$

$$\partial\rho e/\partial t + \nabla\cdot(\rho e\mathbf{u} - \mathbf{q} - \mathbf{u}\cdot\boldsymbol{\tau}) = \mathbf{E}\cdot\mathbf{J} \tag{3}$$

The governing partial differential equation system is identical to the Navier–Stokes equations except for the nonzero source terms. The DCD generated under laboratory conditions has a maximum charged particle number density around $8.8 \times 10^{11}/\text{cm}^3$ over the cathode, and the electrical conductivity is less than 1 mho/m locally [5,7,24]. At an experimental stagnation pressure of 580 torr (7.47 kPa) and a Mach number of 5.15, the air number density in the test section is $1.57 \times 10^{17}/\text{cm}^3$; thus, the mass fraction of the charged particles ranges from 10^{-5} to 10^{-6}, which is merely a trace amount.

The plasma kinetics in atmospheric gases has been studied by Capitelli et al. [25]. Petrusev et al. [26] also investigated the vibration kinetics of nitrogen, including the excitation by electron impact, vibration exchange, and vibrational–translational relaxation. The full 50 quantum levels of nitrogen are considered in the numerical analysis. It was found that the bulk of vibrationally excited molecules mostly take up the lower quantum states, and the level of population decreases rapidly with an increasing vibration quantum number [26]. The detailed mechanism of energy cascading from electronic to vibration excitation is beyond the reach of the present study. For the purpose of applying DCD for flow control, only the dynamics of the weakly ionized air is included. Neglected are the effects of nonequilibrium thermodynamics and chemical kinetics.

The physics of ionization by electron collision is very complex and involves interaction at the atomic level of the gas and solid. The electrons are produced by the avalanche growth from secondary emission. The macroscopic plasma generation process via electron collision at the microscopic scale is accurately described by Townsend's formulation [27,28]. Therefore, a rational model for a direct current discharge needs only to concentrate on the dynamics of the charged particles due to drift motion and diffusion, including ambipolar diffusion [8,16,17]. These properties of the partially ionized plasma are independent of how the gas discharge is generated.

To model the electromagnetic perturbation, a direct current gas discharge model based on the drift-diffusion theory is incorporated. Surzhikov and Shang [8] have successfully developed a model for a three-component (neutral, electron, and ion) and two-temperature, weakly ionized gas. Poggie also adopted this model in his work for shock-wave/boundary-layer interactions for plasma flow control [29]. The basic model, including an externally applied magnetic field, can be given as

$$\partial n_e/\partial t + \nabla\cdot\Gamma_e = \alpha(E,p)|\Gamma_e| - \beta n_+ n_e \tag{4}$$

$$\partial n_+/\partial t + \nabla\cdot\Gamma_+ = \alpha(E,p)|\Gamma_e| - \beta n_+ n_e \tag{5}$$

$$\Gamma_e = n_e\mathbf{u}_\mathbf{e} - D_e\nabla n_e - n_e\mu_e(\mathbf{E} + \mathbf{u}\times\mathbf{B}) \tag{6}$$

$$\Gamma_+ = n_+\mathbf{u}_+ - D_+\nabla n_+ + n_+\mu_+(\mathbf{E} + \mathbf{u}\times\mathbf{B}) \tag{7}$$

In the preceding formulation, $\alpha(E,p)$ and β are the first Townsend ionization coefficient and recombination coefficient. The parameters μ_e and μ_+ are the electron and ion mobilities, and D_e and D_+ are the electron and ion diffusion coefficients [27,28]. When the applied transverse magnetic field is aligned with the z coordinate, the Lorentz acceleration is reduced into two components in x and y coordinates:

$$\mathbf{u}_\mathbf{e}\times\mathbf{B} = u_{e,y}B_z\mathbf{i} - u_{e,x}B_z\mathbf{j} \tag{8}$$

$$\mathbf{u}_+\times\mathbf{B} = \mathbf{u}_{+,y}B_z\mathbf{i} - u_{+,x}B_z\mathbf{j} \tag{9}$$

A compact formulation is achieved by introducing the Hall parameter for electrons and ions as $\beta_e = \mu_e B_z$ and $\beta_+ = \mu_+ B_z$, which are simply the ratios of the cyclotron and averaged charged-and-neutral collision frequencies [22,23]. In the presence of a

transverse magnetic field of B_z, the motions of the charge particles are affected only in the plane that is perpendicular to the applied magnetic field. In practical applications, to achieve the maximum benefit of the Lorentz acceleration, the orientation of the magnetic field is applied perpendicularly to the fluid motion.

The electrical current density that appears in the governing equations (2) and (3) is given by the difference of the charged number flux densities:

$$\mathbf{J} = e(\Gamma_+ - \Gamma_e) \tag{10}$$

A compatible electrical field intensity $\mathbf{E}$ of the discharging domain is obtained by satisfying the charge conservation equation [8]. This equation is further simplified in the globally neutral plasma by introducing an electrical potential function $\mathbf{E} = -\nabla\varphi$. The electric field potential is then the solution of the well-known Poisson equation of plasmadynamics associated with the net space charge density ρ_e:

$$\nabla^2\varphi = -\rho_e/\varepsilon \tag{11}$$

The initial values and boundary conditions, as well as the numerical procedure are directly usable from the cumulative knowledge of the computational fluid dynamics discipline [14,16,17,29]. For the velocity components, the freestream and the no-change condition are prescribed at the entrance, far-field, and exit boundaries of the computational domain, respectively. The no-slip condition applies to all the velocity components on the solid surface. The piecewise isothermal condition is prescribed for the gas temperature on the model and electrode surfaces. Finally, the surface pressure is evaluated by the vanishing normal pressure gradient condition locally.

The initial values and boundary conditions of the plasma model for a numerically stable procedure have been found through a series of sustained research efforts [8,16,17,25,30]. A key element in determining the boundary conditions is specifying the electron number density on the cathode for the secondary emission phenomenon. This physical requirement is met by specifying that the normal component of the electron density flux at the cathode be proportional to its ion counterpart [8]:

$$\Gamma_e \cdot n = -\gamma\Gamma_+ \cdot n \tag{12}$$

Numerical Procedures

All numerical results are obtained by solving the time-dependent governing equations in conservative variables. The interdisciplinary magnetofluiddynamic (MFD) equations (1–3), and the partially ionized plasma model, Eqs. (4), (5), and (11), can be cast into flux vector form:

$$\partial\mathbf{U}/\partial t + \nabla\cdot\mathbf{F} = 0 \tag{13}$$

The dependent variable $\mathbf{U}$ has components of $\{\rho, \rho u, \rho v, \rho w, \rho e, n_e, n_+, \varphi\}$. The detailed description of the flux vectors $\mathbf{F}$ can be found in [16,17], and so they will not be repeated here. In a flux-difference splitting procedure for capturing shock, the flux vectors at the control surface are written as the solution to the approximate Riemann problem:

$$\begin{aligned}\delta\mathbf{F}_i = {} & 1/2[\mathbf{F}(\mathbf{U}_L) + \mathbf{F}(\mathbf{U}_R) - |M_{\text{inv}}|(\mathbf{U}_R - \mathbf{U}_L)]_{i+1/2} \\ & - 1/2[\mathbf{F}(\mathbf{U}_L) + \mathbf{F}(\mathbf{U}_R) - |M_{\text{inv}}|(\mathbf{U}_R - \mathbf{U}_L)]_{i-1/2}\end{aligned} \tag{14}$$

where $\mathbf{U}_L$ and $\mathbf{U}_R$ are interpolated values of the dependent variables, ρ, ρu, ρv, and ρe at interfaces of the control volume, and M_{inv} is the Jacobian matrix of the inviscid or convective terms [31].

A slope limiter is also used to control the discontinuous pressure jumps at the shock front. Time advancement is implicit to resolve the flow, which has a steady-state asymptote. A min-mod limiter is adopted for the present computations:

$$(\mathbf{U}_L)_{i+1/2} = \mathbf{U}_i + 1/4[(1-\kappa)\nabla + (1+\kappa)\Delta]_i \tag{15}$$

$$(\mathbf{U}_R)_{i+1/2} = \mathbf{U}_{i+1} - 1/4[(1-\kappa)\Delta + (1+\kappa)\nabla]_{i+1} \tag{16}$$

In the present application, the value of the parameter κ is assigned a value of one-third to yield a third-order upwind-biased differencing approximation. The min-mod operators are defined as

$$\nabla = \min\text{mod}[\nabla, (3-\kappa)/(1-\kappa)\Delta] \tag{17}$$

$$\Delta = \min\text{mod}[\Delta, (3-\kappa)/(1-\kappa)\nabla] \tag{18}$$

The spatial discretization involves a semidiscrete finite volume scheme [31,32]. The upwind-biasing approximation is applied to the convective and pressure terms. The central differencing is used for the shear stress and heat transfer terms of the governing equations.

All numerical simulations, either for virtual leading-edge strake or virtual variable rectangular cross-sectional area inlet cowls, are three-dimensional. The virtual variable cylindrical inlet is simulated by the axisymmetric formulation. For each group of numerical simulations, a typical two-mesh system was used. For example, two mesh systems of $(85 \times 45 \times 81)$ and $(105 \times 57 \times 101)$ were used for the simulation of the rectangular inlet. To accelerate convergence, three-level mesh sequencing of the multigrid technique is applied [33]. The mesh systems of the half- $(41 \times 23 \times 43)$ and quarter- $(21 \times 12 \times 22)$ mesh number densities are used for the coarser mesh computations. The data processing rate on a 400 MHz SGI Octane2 workstation is 61.6×10^{-6} s per cells per iteration. The convergent criterion of the present analysis is preset at a value of 3.0×10^{-7} for the normalized global residue.

Magnetofluiddynamic Flow Control Mechanism

Hypersonic flow control using the MFD interaction is based on the intrinsic characteristic of the hypersonic similitude parameter of $M\tau$. Any small flow deflection in a supersonic or hypersonic stream will automatically trigger an oblique shock and generate a region of increased pressure over the disturbance. When a DCD is activated, a low-density domain is created immediately adjacent to the discharging electrodes, especially over the cathode. This local expansion leads to a sudden increase of the displacement thickness of the shear layer, which, in turn, induces oblique shock waves over the electrodes.

This phenomenon is easily observed in Fig. 1. The numerical result is generated for the flow condition identical to an experimental effort in a hypersonic MHD channel at a Mach number of 5.15 and a Reynolds number of 2.56×10^5 based on the model length. The DCD is maintained by an applied electrical potential difference of 1.20 kV, and the distance between the embedded electrodes is 2.80 cm. The cathode is placed upstream of the anode at a distance of 2.48 cm from the leading edge. From the computed result, the intensive heat transfer at the edges of the discharge electrodes is clearly and correctly displayed. The Joule heating is concentrated mostly over the cathode; this result is fully substantiated by experimental observation [5,7].

In general, the magnitude of the electromagnetic perturbation generated by DCD is at least 2 orders of magnitude smaller than the aerodynamic inertia and convective heat transfer of a typical hypersonic flow. To become an effective flow control mechanism, the electromagnetic perturbation must be amplified by the viscous–inviscid interaction [16,17,21]. It can be shown that the Joule heating decreases density in the cathode layer to increase the local displacement thickness

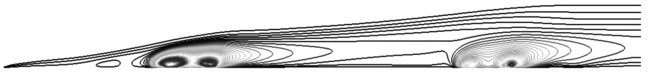

Fig. 1 Temperature contours over DCD on a wedge surface; $M = 5.15$, $Re = 2.57 \times 10^5$, $P = 0.56$ torr, $T = 43$ K, $\varphi = 1200$ V, $I = 60$ mA.

$$\delta^* = \int_0^\infty \left(1 - \frac{\rho u}{\rho_\infty u_\infty}\right) \mathrm{d}y$$

of the boundary layer. The suddenly changing slope of the boundary-layer displacement thickness $\mathrm{d}\delta^*/\mathrm{d}x$ induces a family of compression waves that coalesce into an oblique shock and increases the surface pressure. This phenomenon is clearly illustrated in Fig. 2 by the accompanying computational static temperature profiles over the flat plate surface located midway between electrodes. Both computations are generated at a freestream Mach number of 5.15 and a Reynolds number of 2.56×10^5. According to the experimental condition, at this location, the surface temperature of the model has a constant value of 300 K. When the DCD is activated by an electric potential difference of 1.20 kV, the total electric current in the external circuit is 50 mA. Joule heating appears as an internal heat source to the flowfield and concentrates in the cathode layer. For the boundary layer, the density profile is reciprocal to the temperature profiles and leads to a thickening displacement thickness. Thus, the small electromagnetic perturbation is amplified by the hypersonic viscous–inviscid interaction [21].

Figure 3 presents the schlieren photograph and the computed pressure contours over a sharp leading-edge plate with the activated DCD in a hypersonic MHD flow channel. A dominant feature of the flowfield is the leading-edge shock generated by the hypersonic pressure interaction. The DCD and viscous–inviscid-interaction-induced oblique shock is indicated by both the computational simulation and by experimental observation under the identical condition. The compression wave from the leading edge of the cathode is clearly displayed by both the experimental and the computational results. The weaker induced compression over the anode is resolved only by the numerical simulation, but is not captured by the single-pass schlieren. However, a surface pressure transducer has also recorded the weaker compression over the trailing anode in the experiment [5,7]. At the Mach number of 5.15, the maximum pressure rise over the electrode embedded surface is 1.62 times the freestream value and is 15% higher than the unperturbed counterpart [16,17]. More important, according to the pressure interaction theory, this compression will increase with a higher freestream Mach number [21].

In short, the surface pressure rise for hypersonic flow control using a direct current discharge is derived from a small electromagnetic perturbation to the flowfield and amplified by the viscous–inviscid interaction. In the absence of an externally applied magnetic field, the electromagnetic perturbation is mostly derived from Joule and electrode heating. The increased surface pressure is dependent on the local slope of the displacement thickness of the DCD perturbation and the freestream Mach number [21]. In the absence of an externally applied magnetic field, the electrostatic force due to charge separation near the electrodes has been found to be negligible.

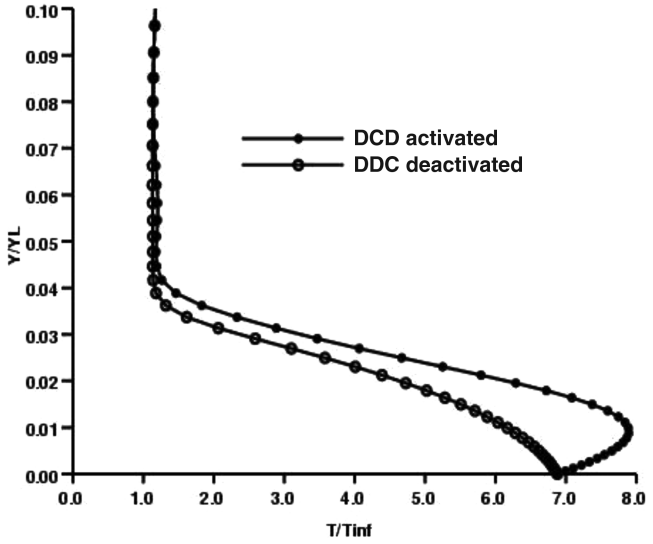

Fig. 2 Comparison of computed static temperature profiles between electrodes with/without activated DCD; $M = 5.15$, $Re = 2.57 \times 10^5$, $P = 0.56$ torr, $T = 43$ K, $\varphi = 1200$ V, $I = 60$ mA.

Validating the Weakly Ionized Gas Model

All experimental data were collected in an MHD channel. This hypersonic low-density facility of the U.S. Air Force Research Laboratory is a blowdown, freejet facility. It is designed to deliver a nominal Mach 5 flow in the test section with a diffuser that achieves at least a normal shock recovery. The simulated altitude, based on the value of flow density, spans a range from 30,000 to 50,000 m. The entire length of the plasma channel is 155.5 cm, and the tunnel exhausts to a 2800 m^3 vacuum sphere. At a fixed stagnation temperature of 270 K, the channel has an operational stagnation pressure range from 0.1 to 1.0 atm [5–7,33,34]. At a typical stagnation pressure of 560 torr (74.7 kPa), the freestream in the test section has a velocity, density, and temperature of 675.5 m/s, 0.0096 kg/m^3, and 43 K, respectively. Under these conditions, the unit Reynolds number in the test section is 2.44×10^6/m.

The detailed behavior of a drift-diffusion DCD model has been investigated continuously [8,16,17,26–29] and has attained good agreement with the classic results of von Engel and Steenbeck [27]. In this work, the partially ionized gas model will be evaluated at the experimental conditions and in an application environment. All of the following presentations focus on validating the DCD model at hypersonic flow conditions of the MHD channel. In other words, the comparison of the model and measured data is conducted at static pressures from 0.59 to 0.93 torr, a static temperature of 43 K, and in the open-jet stream moving at 675.5 m/s.

In Fig. 4, the computed global characteristics of the DCD are compared with experimental observations in a uniform transverse magnetic field from −0.05 to 0.05 T [5,7,24]. The applied magnetic

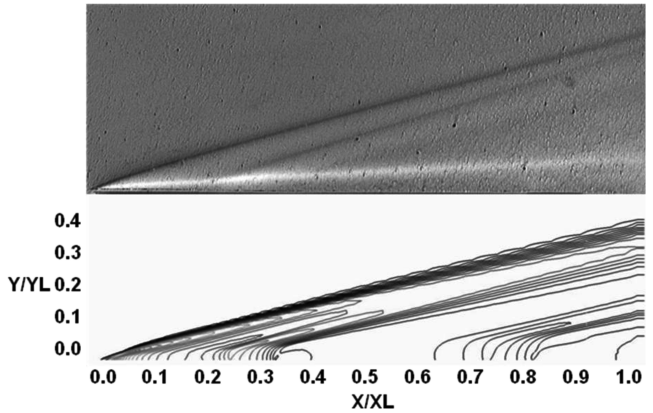

Fig. 3 Comparison of induced shock structure for activated DCD; $M = 5.15$, $Re = 2.57 \times 10^5$, $P = 0.56$ torr, $T = 43$ K, $\varphi = 1.2$ V.

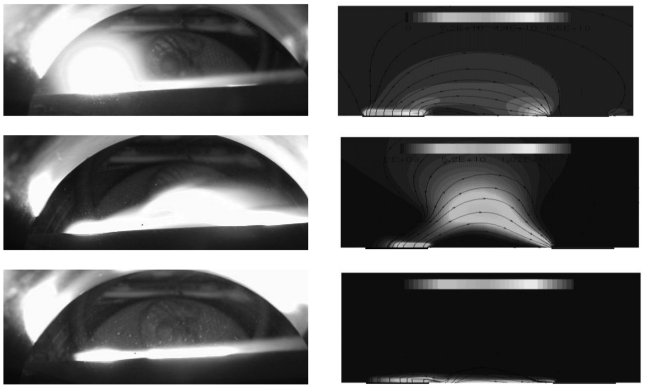

Fig. 4 Simulate DCD in transverse magnetic field; $-0.05 < B < 0.05$ T, emf = 1.2 kV, $P = 5.0$ torr (top to bottom: $B = 0.0$ T, $B = -0.05$ T, and $B = +0.05$ T).

field is applied transversely to the flow, along or opposite of the z coordinate. The discharge is sustained by an electric potential difference around 840 V and a current less than 100 mA. For numerical simulations, the Hall parameters for electrons and ions are 0.44 and 0.0145, respectively. The electrical current traces from the computational results are also included in the presentation to identify the local direction of the Lorentz force.

In a side-by-side electrode arrangement, the cathode is placed upstream (on the left) of the anode and with a separation distance of 3.81 cm. The essential physics of the DCD is captured by the drift-diffusion model; the intensive glow associated with the transition of charged particles is duplicated by the computational simulations. Most importantly, the dominant effect of the Lorentz acceleration stands out. The vector trace of the computed discharging electric current is included in the composite graph to identify the orientation of the Lorentz force. The positive transverse field (along the z coordinate or point out from the graph) $B = +0.05$ generates a suppressing force to restrain the upward movement of the electrons, which is displayed in the bottom row of the figure. When the polarity is reversed (along the negative z coordinate or point into the graph), $B = -0.05$, the computational result in the middle row exhibits an opposite pattern. The Lorentz force under this condition expels the electrons away from the electrodes. In essence, the physically based model with a transverse magnetic field duplicates the essential discharge physics. The specific quantification of the Lorentz force to the DCD will be discussed in a later section.

The specific comparison of the charge particles profile with experimental data is depicted in Fig. 5. The glow discharge is maintained by an electrical potential difference of 1.2 kV at an ambient pressure of 0.59 torr (78.4 Pa). The studied side-by-side electrode configuration is identical to that for investigating the Lorentz force in the presence of the externally applied magnetic field. It is well known that charge separation takes place in the cathode layer, and the ion number density can be as high as 3 times or more than the electron density. The computed ion number density distribution above the anode has a general agreement with experimental data [16,17]. The computed ion and electron number density beyond the cathode and anode layer is $9.8 \times 10^8/\text{cm}^3$ and correctly reflects the globally neutral property of the plasma. The discrepancy between the data and the computational results is within the data disparity acquired by Langmuir probes and by microwave absorption technique in a high-speed flow environment [5,7].

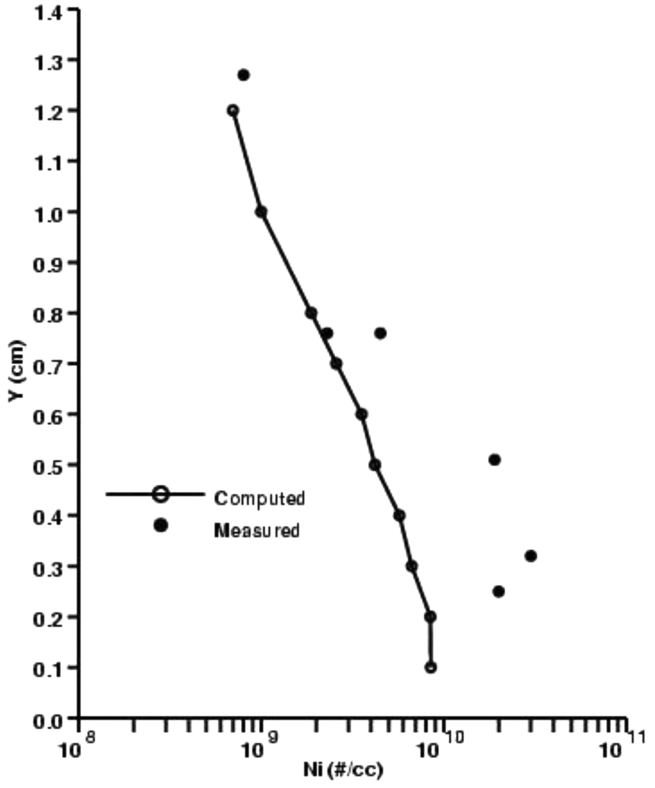

Fig. 5 Validate charged particles density with data; $M = 5.15$, $Re = 2.57 \times 10^5$, $P = 0.56$ torr, $T = 43$ K, $\varphi = 1200$ V, $I = 60$ mA.

The simulation using the drift-diffusion model also produces a reasonable agreement with the measurement obtained by a stagnation temperature probe [7]. In Fig. 6, the comparison is given in a dimensionless value normalized by the freestream temperature (43 K). The size of the sheltered probe and its aerodynamic interference prevents accurate measurements within both the cathode and the anode layers. The most noticeable feature of the computational results is that the Joule heating is dominant. The gas temperature near the wall is actually higher than the surface temperatures of the cathode and anode. In fact, the cathode has attained a temperature that exceeds 460 K, mostly by the electrode heating [5–7].

From previous evaluations with the classic parallel electrode configuration by Surzhikov and Shang [8], von Engel and Steenbeck [27], and with the present validating process [16,17], the drift-diffusion model has demonstrated the ability to describe the essential physics of a DCD for flow control. Additional validation of the discharge physics simulation in charged particles density prediction must be continued into the future.

Virtual Leading-Edge Strake

In Fig. 7, the DCD over a sharp leading-edge wedge in a Mach 5.15 hypersonic stream is displayed. The near-surface plasma is generated by two electrodes embedded in the flat plate surface of the wedge. A total electrical current of 50 mA is maintained by an applied electric field of 1.2 kV in the external circuit. The maximum

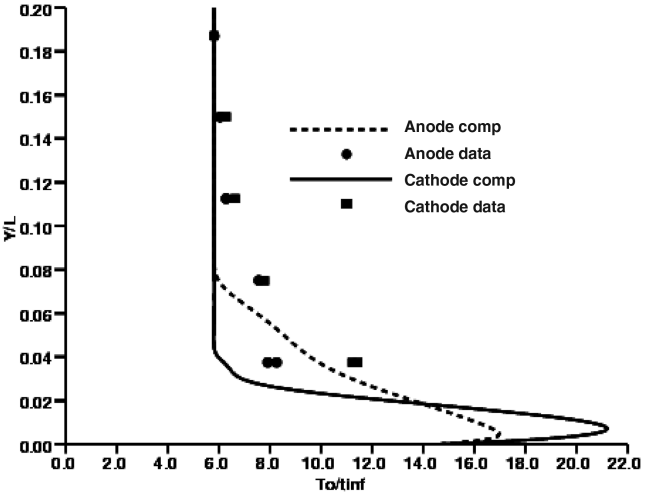

Fig. 6 Verify stagnation temperature profile with data; $M = 1.5$, $Re = 2.57 \times 10^5$, $T = 43$ K, $P = 0.56$ torr, $Pw = 64$ W.

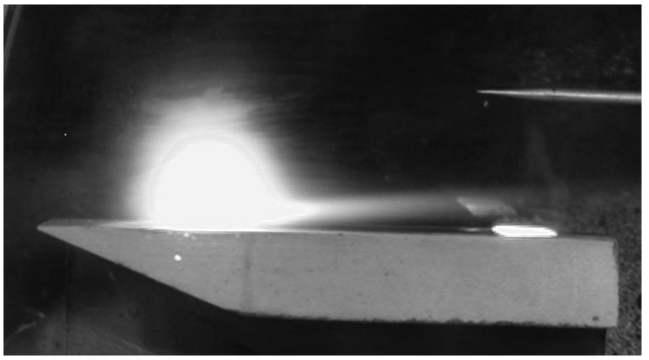

Fig. 7 DCD over a wedge; $M = 5.15$, $Re = 2.57 \times 10^5$, $P = 0.56$ torr, $T = 43$ K.

electron number density of the plasma is $3 \times 10^{11}/\text{cm}^3$, and the electrode temperature is estimated to be 460 K [5,7,24]. At a freestream pressure of 0.59 torr and a static temperature of 43 K, the air density is $1.33 \times 10^{17}/\text{cm}^3$, the degree of ionization is 2.25×10^{-5}, and the electrical conductivity is on the order of 1 mho/m. In the hypersonic viscous–inviscid interacting domain, the glow discharge provides a truly weakly ionized gas over the electrodes but operates in the abnormal mode. A visible fluctuating discharging pattern was often observed when DCD was activated.

The relative importance of the surface convective and volumetric Joule heating is confirmed by experimental and computational results. In Fig. 8, solutions of the MFD equations using the drift-diffusion model are compared with measurements at the Mach number of 5.15 and Reynolds number of 2.57×10^5. Numerical results were generated over the wedge model by the actuated DCD and by heating electrodes to the discharging temperature of 460 K, all of which exhibit reasonable agreement with data. Most important, the glow discharge induces a bona fide electroaerodynamic interaction that is not possible with electrode heating alone [16,17]. At a very low-level power of 50 W, the electroaerodynamic interaction generates a pressure rise on the wedge surface equivalent to a 1 deg angle of attack of the surface at Mach 5.15. From this result and a series of experiments with increasing plasma power input was performed. It was found that the scaling of power required for the plasma actuator per electrode area is about $9.17\ \text{W} \cdot \text{cm}^{-2}/\text{deg}$.

The effect of the Lorentz force is easily detected from the computed surface pressure over the electrodes in Fig. 9. The DCD is maintained by an electric potential difference of 1.2 kV and at a circuit current of 50 mA. The computed results were generated at a typical running condition of the MHD channel; the stagnation pressure and temperature are 580 torr (77.3 kPa) and 270 K, respectively. The Lorentz force is relatively small, about $\pm 0.02\ \text{N/m}^3$ at the externally applied uniform magnetic field of ± 0.2 T. The computed result generally overpredicts the pressure measurement, and the measured data also exhibit an unusually large data scattering due to the unstable glow discharge in the presence of an applied magnetic field. The expelling Lorentz force ($\mathbf{J} \times \mathbf{B} < 0$, $B = -0.2$ T) indeed pushes the charged particles away from the electrodes and increases the collision for momentum transfer. Thus, the induced surface pressure is greater than the MFD interaction without the presence of a transverse magnetic field, but at identical electric field intensity. The trend of increasing the discharge domain is reversed with the opposite magnetic polarity ($\mathbf{J} \times \mathbf{B} > 0$, $B = +0.2$ T). The induced surface pressure is also diminished accordingly by suppressing the outward deflection of the streamline. It is interesting to note that increased effort was required to maintain the computational stability. Nevertheless, the numerical results using the drift-diffusion model capture the difference between the applied magnetic fields of opposite polarities [30].

The validated numerical simulations also illustrate the profound influence of a relatively small applied magnetic field to the flow control effectiveness. In fact, a transverse magnetic field of 0.2 T, aligning with the reverse direction of the z coordinate, has generated a 34% higher pressure level on the control surface than that without the externally applied magnetic field [16,17]. The control effectiveness is greatly enhanced by the Lorentz force.

The magnetofluiddynamic interaction produces a high-pressure region between the electrodes. The high surface distribution over the immobile wedge with an activated DCD acts as if the surface had executed a pitching motion: the performance identical to a movable leading-edge strake. A series of calculations with the discharge current from 50 to 350 mA yields the equivalent angles of attack from 1 to exceeding 5 deg for the deployed virtual strake. Meanwhile, beyond the discharge current of 350 mA, the glow discharge transits into an arc. The computed results are substantiated by experimental data, as depicted in Fig. 10 [17].

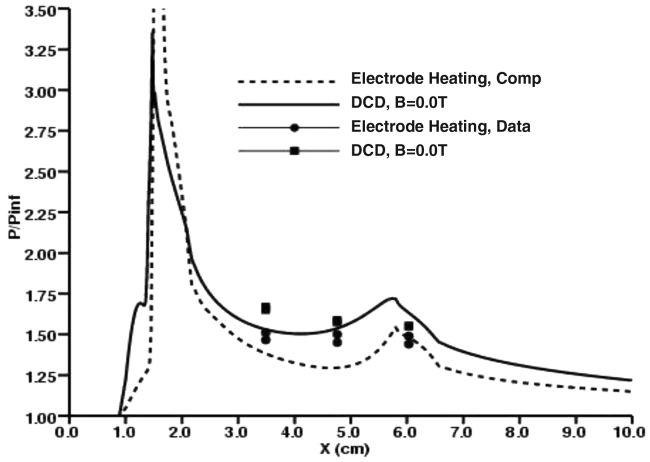

Fig. 8 Surface pressure distribution over wedge with/without DCD; $M = 5.15$, $Re = 2.57 \times 10^5$, $P = 0.56$ torr, $T = 43$ K [17].

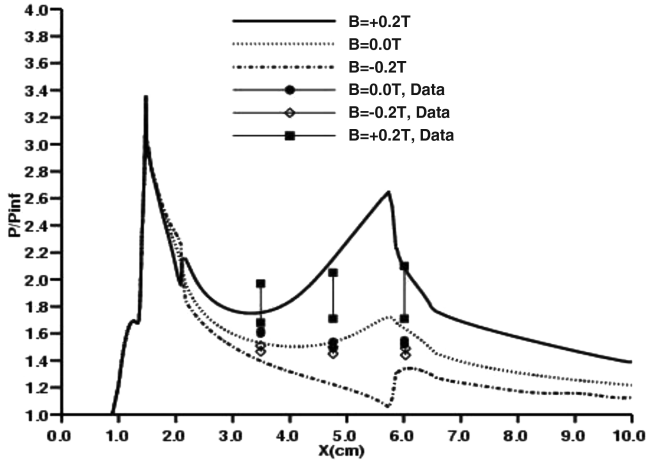

Fig. 9 Surface pressure distribution with DCD and transverse magnetic field; $M = 5.15$, $Re = 2.57 \times 10^5$, $P = 0.56$ torr, $T = 43$ K.

Virtual Variable Geometrical Inlet Cowls

The magnetofluiddynamic interaction is equally applicable as a virtual variable geometrical inlet cowl using the amplified electromagnetic perturbation. Computational and experimental efforts for the constant cross-sectional area rectangular and cylindrical inlets were carried out. These two inlets are designed for nearly identical cross-sectional area and the same total length, to assess the relative merit of the improved aerodynamic performance,

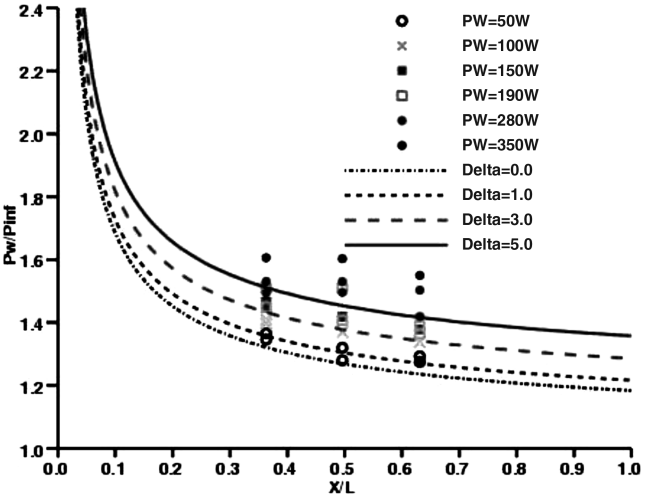

Fig. 10 Power scaling of DCD virtual leading-edge strake; $M = 5.15$, $Re = 2.57 \times 10^5$, $P = 0.56$ torr, $50 < Pw < 350$ W [17].

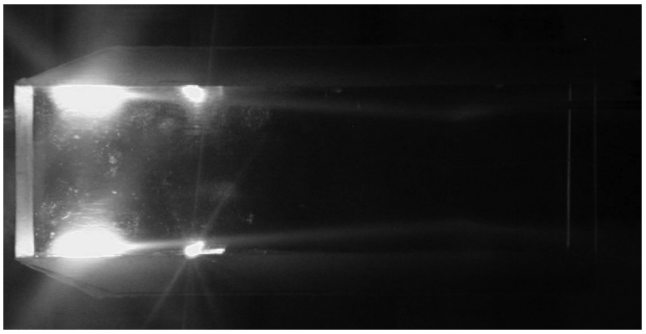

Fig. 11 DCD from side-by-side electrodes of a rectangular inlet; $M = 5.15$, $Re = 2.57 \times 10^5$, $P = 0.56$ torr, $T = 43$ K, $Pw = 64$ W [34].

and for the difference between a three-dimensional and an axisymmetric configuration.

The top view of the discharge pattern with the side-by-side electrode is presented in Fig. 11. The four embedded electrodes have the same dimensions of 2.03 cm^2, and the cathodes are placed at 0.64 cm from the inlet leading edge upstream of the anode. The separation distance between electrodes is 2.22 cm. At the static pressure of 0.56 torr, the discharges are maintained at electric potentials from 480 to 800 V, with electric current from 40 to 80 mA. Therefore, the electric current density has a value of 21.8 mA/cm^2 over the anode, and the near-surface plasma is generated by a total power input of 64 W within the hypersonic inlet.

The density contours in the x-y plane of the rectangular inlet are given in Fig. 12. It can be easily seen that the DCD strengthens the oblique shock, which originated from the viscous–inviscid interaction at the sharp leading edges of the inlet. The oblique shocks from the sidewalls intersect each other at $x/L = 0.60$, upstream to that of the weaker oblique shocks originating from the top and bottom surfaces [32]. The MFD compression is the consequence of the Joule and electrode heating, which alters the boundary-layer displacement thickness on the side walls. An estimated 12 W of the power used for plasma generation is converted into Joule heating; this value is in general agreement with the estimate by nonequilibrium chemical kinetics, including energy cascading between the internal degrees of freedom of the weakly ionized gas [24,26].

The shock structure induced by the DCD is rather complex; the mutually perpendicular leading edge and the embedded electrodes generate four oblique shocks over the inlet surface. Immediately downstream of the electrodes, a total of eight triplet points of the intersecting oblique shocks are detected by both computational and experimental means [33,34]. The interacting flowfield is simulated by solving the MFD equations on two mesh systems of $(85 \times 45 \times 81)$ and $(105 \times 57 \times 101)$. However, the major portions of the results are generated on the fine mesh and with a three-level multigrid sequence to accelerate convergence. The oblique shock waves eventually intersect each other, reflect from the side walls, and finally dissipate. For the rather complex MFD-induced compression, the computational results provide a consistent prediction of the interacting phenomenon, as shown in Fig. 13. When DCD is activated, the strengthened oblique shock produces a persistent higher pitot pressure (a maximum of 14.3%) than the

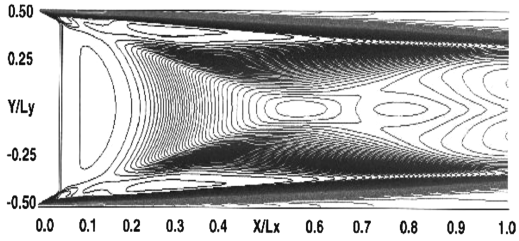

Fig. 12 Joule heating distribution; $M = 5.15$, $Re = 2.57 \times 10^5$, $P = 0.56$ torr, $T = 43$ K, $\varphi = 800$ V, $I = 60$ mA.

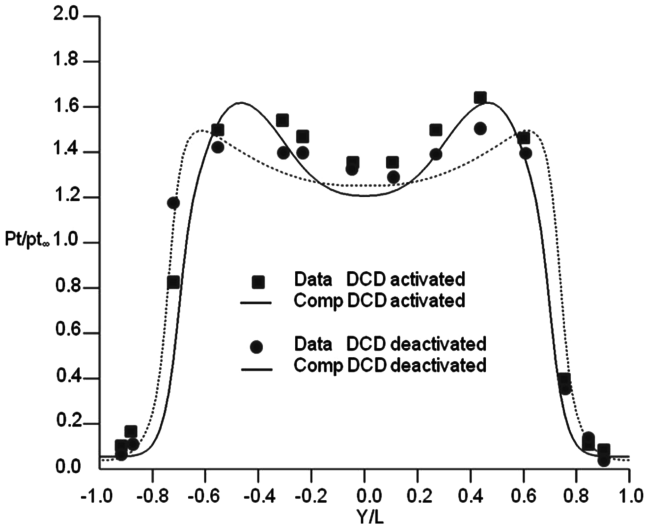

Fig. 13 Comparison of pitot pressure profiles at exit plane of rectangular inlet; $M = 5.15$, $Re = 2.57 \times 10^5$, $P = 0.56$ torr, $\varphi = 800$ V, $I = 80$ mA.

unperturbed counterpart. The comparison of the computed and measured pitot pressure profiles on the center plane has a reasonable agreement near the exit of the inlet. At this location, the MFD-induced oblique shocks from the sidewall discharge are still predominant.

Figure 14 presents the comparison of experimental and computed pitot pressures along the centerline of the rectangular inlet when the DCD is either activated or deactivated. Both results generated at a stagnation pressure of 580 torr have captured the interacting oblique shocks within the inlet [33,34]. Here, the circular symbols and dashed line correspond to the results of the deactivated discharge, and the square symbols and solid line denote the results from the activated discharge. When the DCD is actuated, the induced oblique shock becomes steeper and moves the interception of the shock waves upstream. The ensured expansion follows the strengthened shock and produces a slightly lower pitot pressure along the centerline downstream. The actuated DCD leads to a higher peak pitot pressure and an upstream movement, in contrast to its deactivated counterpart. The computed results have good agreement with the experimental data. The computations underpredict the peak pitot pressure by 2% and overpredict the uniform entrance condition by 1.2%. This small discrepancy in magnitude is directly attributable to the fluctuating DCD and the uncertain Mach number at the entrance of the inlet due to model blockage.

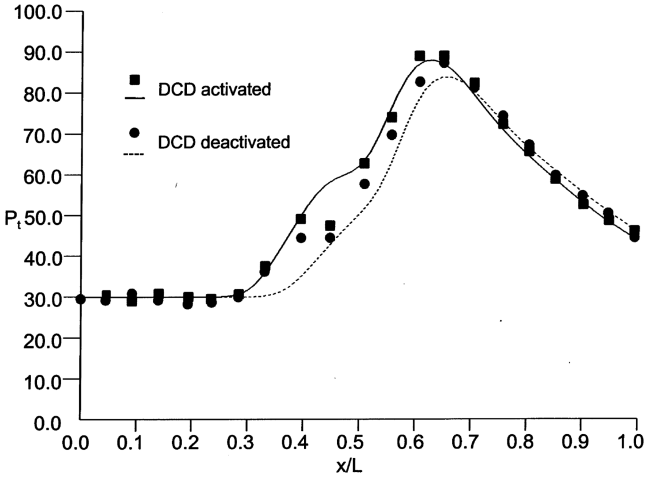

Fig. 14 Comparison of pitot pressure along centerline of rectangular inlet; $M = 5.15$, $Re = 2.57 \times 10^5$, $P = 0.56$ torr, $\varphi = 800$ V, $I = 80$ mA.

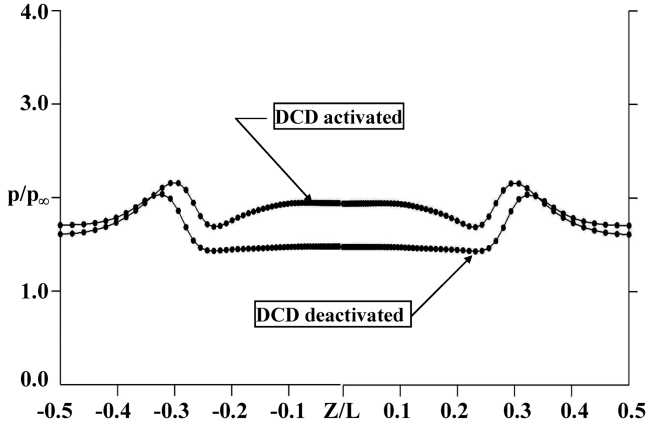

Fig. 15 Static pressure profiles in *x*-*z* plane at exit of rectangular inlet with/without DCD; $M = 5.15$, $Re = 2.57 \times 10^5$, $P = 0.56$ torr, $\varphi = 800$ V, $I = 80$ mA [34].

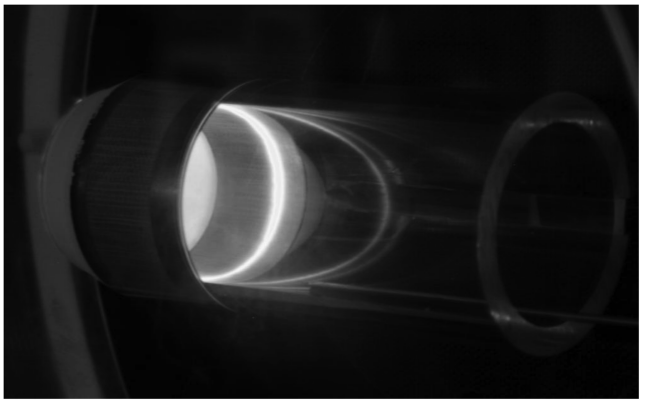

Fig. 17 DCD over the leading edge of cylindrical inlet model; $M = 5.15$, $Re = 2.58 \times 10^5$, $P = 0.96$ torr, $Pw = 64$ W.

Figure 15 presents the comparison of computed static pressure distributions in the *x*-*z* plane near the inlet exit. The difference in pressure distributions with and without the activated DCD is similar to that in the *x*-*y* plane, except the pressure level is consistently higher by the induced vertical sidewall compression over most of the inner core region. Because the electrodes are embedded in the vertical sidewalls, there is no additional compression from these horizontal surfaces. The increased static pressure is the result of the MFD interaction originating from the entrance of the inlet. The averaged static pressure over the entire exit cross-sectional area is 11.7% greater than its counterpart without electromagnetic perturbation [34].

The effectiveness of MFD compression in a constant area rectangular inlet at different freestream Mach numbers is depicted in Fig. 16. Four numerical simulations are included at Mach numbers of 5.0 and 6.0; the actuated DCD produces a greater compression than the deactivated flows. At a higher Mach number, the energy input for plasma generation is kept at the same value as that for the lower Mach number flow. At the higher freestream velocity, 810.6 versus 675.5 m/s, energy is more dissipated into the airstream [33,34]. Therefore, the electromagnetic perturbation is diminished and, consequently, the MFD compression is not increased according to the cube power of the Mach number. However, a higher compression can be recovered by increasing the electric current density of the DCD.

A photograph of the ignited DCD in the cylindrical inlet is presented in Fig. 17. The discharge is sustained by an applied electric potential of 460 V and a current of 150 mA. Experimental data were collected at two different stagnation pressures (580 and 370 torr), which correspond to two Reynolds numbers of 1.66×10^5 and 2.57×10^5. The DCD is viewed from the inlet exit and at an oblique angle from the axis. The dominant visual feature of the discharge is the glow over the electrodes and the reflection from the model sidewalls. Under this testing condition, the discharge current density on the anode is 6.78 mA/cm^2; this value is nearly 3 times lower than that of the rectangular inlet with a different electrode arrangement [33–35]. For this reason, the DCD pattern of the cylindrical inlet is essentially fluctuation free. This behavior persists even when the circuit current density on the anode reaches a value of 20.34 mA/cm^2 by increasing circuit current to 150 mA. For this reason, the experimental measurements of this configuration have a significantly reduced data scatter than the previous results for a rectangular inlet [34].

The density contours of the deactivated and the actuated DCD in the constant cross section cylindrical inlet are presented in Fig. 18. The cylindrical inlet has an inner diameter of 3.50 cm and is designed to have a comparable cross-sectional area to the rectangular inlet of 11.8 cm^2. The entire flowfield is dominated by a convergent and divergent conical shock, which is induced by the pressure interaction at the leading edge. The comparative study consists of two computed results: on the lower half-plane is the baseline case with the deactivated DCD, and, on the upper half-plane, the solution is generated with the actuator powered by 69.0 W, the applied electric field potential is 460 V, and the circuit current is 150 mA. When the DCD is activated, the strengthened oblique shock impinges on the inner surface of the inlet downstream of the shock focus. At the lower Reynolds number condition $Re = 1.66 \times 10^5$, the impinging shock generates an unexpected and additional shock–boundary-layer interaction near the exit. The numerical simulation shows that the adverse pressure gradient even triggers incipient flow separation near

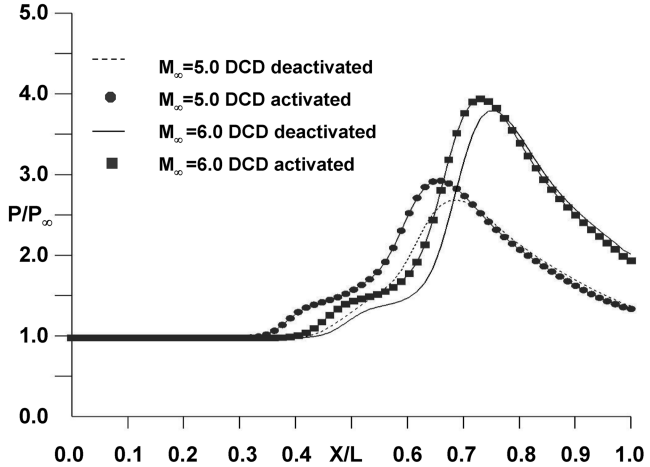

Fig. 16 Magnetofluiddynamic compression at different Mach numbers; $Re = 2.57 \times 10^5$, $Pw = 64$ W Ref. [34].

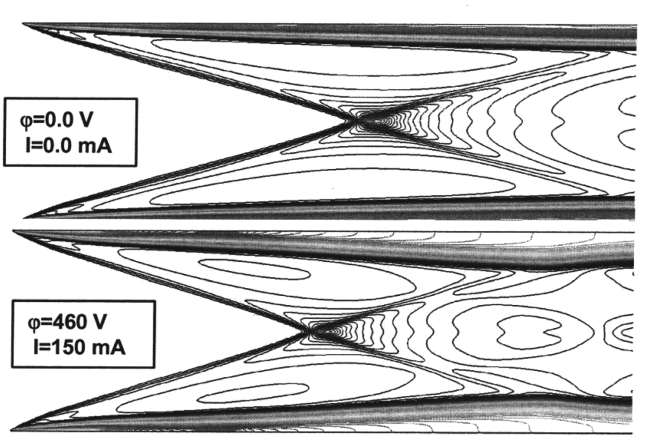

Fig. 18 Density contours of the cylindrical inlet with/without the activated DCD; $M = 5.15$, $Re = 2.58 \times 10^5$, $P = 0.96$ torr, $T = 43$ K, $\varphi = 460$, $I = 150$ mA.

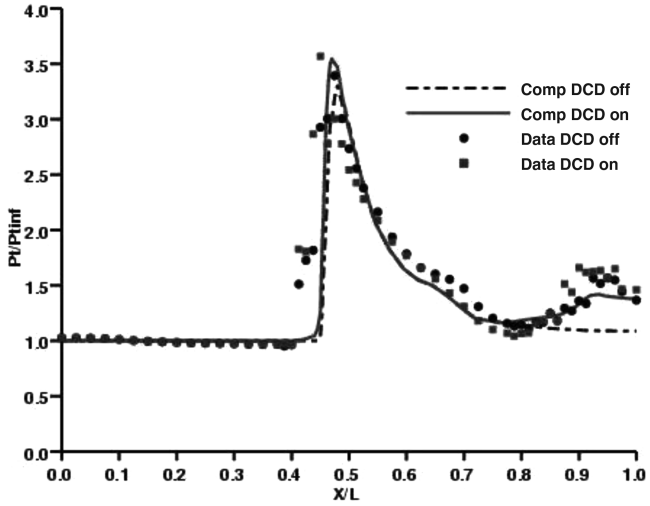

Fig. 19 Impact pressure distributions along the axis of the cylindrical inlet; $M = 5.15$, $Re = 1.66 \times 10^5$, $P = 0.96$ torr, $T = 43$ K, $\varphi = 480$, $I = 150$ mA.

the exit plane. This result is partially verifiable through the experimental observations in pitot pressure measurements [35].

This specific phenomenon is further verified in Fig. 19 at the Reynolds number of 1.66×10^5 by the comparison of the streamwise pitot pressure distributions along the axis of the model. The computed and measured results of the actuated DCD are designated by the solid line and filled square symbols and by the dashed line and the filled circles for the unperturbed condition. The computing simulations do not include the slightly blunt leading edge and thus have a weaker oblique shock. As a consequence, the shock focus is consistently formed downstream of the experimental observation. More important, the divergent conical shock, after passing through the shock focus, does not impinge on the inlet sidewall. However, the shock of the experiments impinges on the sidewall and creates an adverse pressure gradient near the inlet exit, which has induced an incipient flow separation and unsteady flow at the same Reynolds number condition. This behavior is different from the numerical simulations of the cylindrical inlet with a sharp leading edge, in which the divergent shock exits the inlet uninterrupted.

The important and precise comparison of pitot pressure profiles near the cylindrical inlet exit plane is prevented by the unsteady or separated flow behavior at the inlet exit. Two sets of data taken on different days exhibit a much larger scattering in comparison with computing results at a streamwise location of $X/D = 3.8$, the inlet exit. In Fig. 20, the computational simulations with and without DCD

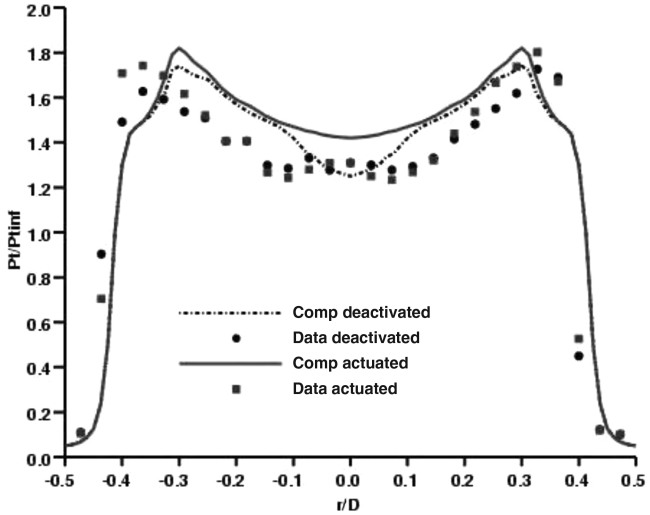

Fig. 20 Pitot pressure profiles at exit of the cylindrical inlet; $M = 5.15$, $Re = 2.58 \times 10^5$, $\varphi = 480$ V, $I = 150$ mA.

actuation are embedded within the data bands of the cylindrical inlet experiments. Nevertheless, the computational simulations of the cylindrical inlet indicate a definitive but smaller gain in MFD compression than that of the rectangular configuration. From the computational investigation and verified experimental data on the virtual inlet cowl, the DCD in a rectangular inlet has produced an additional MFD compression of 11.7% compared with its unperturbed counterpart with a plasma generation power of 64 W [33,34]. The DCD in the cylindrical inlet produces less compression; 6.7% less under the identical freestream conditions at a Mach number of 5.15 and Reynolds number of 2.57×10^5. The lower compression has two distinct contributors. First, the electric current density is much lower in the electrode configuration for the cylindrical inlet. Second, the intrinsic difference in spatial dimension plays a role in the difference between the rectangular three-dimensional and the axisymmetric configuration, in that the Mangler scale of $\sqrt{3}$ actually reduces the outward displacement thickness of the electromagnetic perturbation. In summary, the DCD generates a lower MFD compression for the axisymmetric inlet. The MFD compression is generated at low power for plasma generation, 2.8 W/cm^2.

Conclusions

A viable application of plasma actuators for flow control in the hypersonic regime has been demonstrated by computational analysis using the magnetofluiddynamic equation in the low magnetic Reynolds number limit with a plasma model. The key mechanism of an effective plasma actuator for flow control is the amplification of an electromagnetic perturbation by the unique hypersonic pressure interaction. The basic approach introduces a direct current discharge near the sharp leading edges of the inlet, thereby altering the slope of the shear layer thickness, which results in a stronger viscous–inviscid interaction. This conclusion is fully substantiated by experimental observations.

In application as a virtual leading-edge strake, the magnetofluiddynamic interaction creates a pressure plateau on a fixed surface that is equivalent to a movable control surface pitching up to 5 deg at the freestream Mach number of 5.15. An externally applied transverse magnetic field increases the surface pressure rise by a factor of 1.34. The effectiveness of the virtual leading-edge strake is reflected by an averaged power scaling of 9.17 W $\cdot$ cm^{-2}/ deg.

The magnetofluiddynamic compression performs equally well as a virtual cowl that enhances the performance of constant cross section inlets. Under the investigated condition of Mach 5.15 and a Reynolds number of 2.57×10^5, the magnetofluiddynamic sidewall compression within a rectangular inlet produces an 11.7% gain by a plasma generating power input of 4.4 W/cm^2 from electrodes. In this aspect, the present approach using a plasma actuator for hypersonic flow control has overcome the fundamental inefficient ionization process.

The numerical results also show that the effectiveness of a virtual variable geometry cowl can increase with higher freestream Mach numbers, if the intensity of the DCD can be sustained. Detailed and optimal electrode placement in the inlet becomes pivotal for a versatile and widely applicable virtual inlet cowl. Research efforts in this area shall be continued.

The induced magnetofluiddynamic compression in a cylindrical inlet is determined to be 6.7% over that of the unperturbed counterpart. The reduced compression in comparison with the three-dimensional inlet is mainly due to the reduced electric current density (6.25 mA/cm^2) of the DCD and the Mangler effect of the axisymmetric configuration. Under this circumstance, the MFD compression gain is achieved without any loss of the stagnation pressure by the virtual variable inlet cowl.

Acknowledgments

The support of F. Fahroo and J. D. Schmisseur of the U.S. Air Force Office of Scientific Research is deeply appreciated. The author is thankful for the fruitful exchange with and earnest support of D. Gaitonde, R. Kimmel, and J. Hayes of the U.S. Air Force Research

Laboratory, as well as his colleagues at Wright State University, J. Menart and G. Huang. Last but not least, the author highly values his collaboration with S. Surzhikov of the Russian Academy of Science, Moscow.

References

[1] Bityurin, V., Kilmov, A., Leonov, S., Lutsky, A., Van Wie, D., Brovkin, V., and Kolesnichenko, Yu., "Effect of Hetrogenous Discharge Plasma on Shock Wave Structure and Propagation," AIAA Paper 99-4940, 1999.

[2] Leonov, S., Bityurin, V., Savelkin, K., and Yarantsev, D., "Effect of Electrical Discharge on Separation Processes and Shock Position in Supersonic Airflow," AIAA Paper 2002-0355, Jan. 2002.

[3] Bityurin, V. A., Bocharov, A. N., and Lineberry, J. T., "Results of Experiments on MHD Hypersonic Flow Control," AIAA Paper 2004-2263, June 2004.

[4] Macheret, S. O., Shneider, M. N., and Miles, R. B., "Magneto-hydrodynamic Control of Hypersonic Flows and Scramjet Inlets Using Electron Beam Ionization," *AIAA Journal*, Vol. 40, No. 1, 2002, pp. 74–81.

[5] Menart, J., Shang, J., Kimmel, R., and Hayes, J., "Effects of Magnetic Fields on Plasmas Generated in a Mach 5 Wind Tunnel," AIAA Paper 2003-4165, June 2003.

[6] Shang, J. S., and Surzhikov, "Magneto-Fluid-Dynamics Interaction for Hypersonic Flow Control," AIAA Paper 2004-0508, Jan. 2004.

[7] Kimmel, R., Hayes, J., Menart, J., and Shang, J., "Effect of Surface Plasma Discharges on Boundary Layer at Mach 5," AIAA Paper 2004-0509, Jan. 2004.

[8] Surzhikov, S. T., and Shang, J. S., "Two-Component Plasma Model for Two-Dimensional Glow Discharge in Magnetic Field," *Journal of Computational Physics*, Vol. 199, No. 2, Sept. 2004, pp. 437–464. doi:10.1016/j.jcp.2004.02.019

[9] Borghi, C. A., Carraro, M. R., and Cristofolini, A., "An Axisymmetric Hall Configuration for MHD Interaction in Hypersonic Flows," AIAA Paper 2005-4785, June 2005.

[10] Cristofolini, A., Borghi, C. A., Carraro, M. R., Neretti, G., Biagioni, L., Fantoni, G., and Passaro, A., "Experimental Investigation on the MHD Interaction Around a Sharp Cone in an Ionized Argon Flow," AIAA Paper 2006-3075, June 2006.

[11] Bletzinger, P., Ganguly, B. N., Van Wie, D., Garscadden, A., "Plasmas in High-Speed Aerodynamics," *Journal of Physics D: Applied Physics*, Vol. 38, No. 4, 2005, pp. R33-R57. doi:10.1088/0022-3727/38/4/R01

[12] Leonov, S. B., Yarantsev, D. A., Gromov, V. G., and Kuriachy, A. P., "Mechanisms of Flow Control by Near-Surface Electrical Discharge Generation," AIAA Paper 2005-0780, Jan. 2005.

[13] Leonov, S. B., Yarantsev, D. A., and Soloviev, V. R., "Experiments on Control of Supersonic Flow Structure in Model Inlet by Electric Discharge," AIAA Paper 2007-3890, June 2007.

[14] Gaitonde, D. V., "Simulation of Local and Global High-Speed Flow Control with Magnetic Fields," AIAA Paper 2005-0560, Jan. 2005.

[15] Nishihara, M., Jiang, N., Lempart, W. R., Adamovich, I. V., and Gogineni, S., "MHD Supersonic Boundary Layer Control Using Pulsed Discharge Ionization," AIAA Paper 2005-1341, Jan. 2005.

[16] Shang, J. S., and Surzhikov, S. T., "Magnetoaerodynamic Actuator for Hypersonic Flow Control," *AIAA Journal*, Vol. 43, No. 8, Aug. 2005, pp. 1633–1643. doi:10.2514/1.6625

[17] Shang, J. S., Surzhikov, S. T., Kimmel, R., Gaitonde, D. V., Hayes, J. R., and Menart, J., "Mechanisms of Plasma Actuators for Hypersonic Flow Control," *Progress in Aerospace Sciences*, Vol. 41, No. 8, Nov. 2005, pp. 642–668. doi:10.1016/j.paerosci.2005.11.001

[18] Shang, J. S., "Electromagnetic Field of Dielectric Barrier Discharge," *36th Plasmadynamics and Laser Conference*, AIAA Paper 2005-5182, June 005.

[19] Boeuf, J. P., Lagmich, Y., Callegari, Th., and Pitchford, L. C., "Electrohydrodynamic Force and Acceleration in Surface Discharge," AIAA Paper 2006-3574, 2006.

[20] Lieberman, M. A., and Lichtenberg, A. J., *Principles of Plasma Discharges and Materials Processing*, Wiley, New York, 1994.

[21] Hayes, W. D., and Probstein, R. F., *Hypersonic Flow Theory*, Academic Press, New York, 1959.

[22] Sutton, G. W., and Sherman, A., *Engineering Magnetohydrodynamics*, McGraw–Hill, New York, 1965, pp. 295–308.

[23] Mitchner, M., and Kruger, C. H., Jr., *Partially Ionized Gases*, Wiley, New York, 1973, pp. 188–198.

[24] Kimmel, R. L., Hayes, J. R., Menart, J. A., and Shang, J. S., "Effect of Magnetic Fields on Surface Plasma Discharges at Mach 5," *Journal of Spacecraft and Rockets*, Vol. 43, No. 6, 2006, pp. 1340–1346. doi:10.2514/1.14247

[25] Capitelli, M., Ferreira, C. M., Gordiets, B. F., and Osipov, A. I., *Plasma Kinetics in Atmospheric Gases*, Springer, Berlin, 2000, pp. 229–246.

[26] Petrusev, A. S., Surzhikov, S. T., and Shang, J. S., "A Two-Dimensional Model of Glow Discharge in View of Vibrational Excitation of Molecular Nitrogen," *High Temperature*, Vol. 44, No. 6, 2006, pp. 804–813. doi:10.1007/s10740-006-0097-9

[27] von Engel, A., and Steenbeck, M., *Elektrische Gasenladungen*, Vol. 2, Springer, Berlin, 1932.

[28] Raizer, Yu. P., and Surzhikov, S. T., "Diffusion of Charges Along Current and Effective Numerical Method of Eliminating of Numerical Dissipation at Calculations of Glow Discharge," *High Temperature*, Vol. 28, No. 3, 1990, pp. 324–328.

[29] Poggie, J., "Plasma-Based Control Shock-Wave/Boundary-Layer Interaction," AIAA Paper 2006-1007, 2006.

[30] Surzhikov, S. T., and Shang, J. S., "The Hypersonic Quasineutral Gas Discharge Plasma in a Magnetic Field," *Proceedings of the Third MIT Conference on Computational Fluid and Solid Mechanics*, Elsevier Science, Amsterdam, 2005, pp. 1004–1005.

[31] Rumsey, C., Biedron, R., and Thomas, J., "CFL3D: Its History and Some Recent Applications," NASA TM-112861, May 1007.

[32] Thomas, J. L., Diskin, B., Brandt, A., "Textbook Multigrid Efficiency for Fluid Simulation," *Annual Review of Fluid Mechanics*, Vol. 35, Jan. 2003, pp. 317–340. doi:10.1146/annurev.fluid.35.101101.161209

[33] Shang, J. S., Menart, J., Kimmel, R., and Hayes, J., "Hypersonic Inlet with Plasma Induced Compression," AIAA Paper 2006-0764, Jan. 2006.

[34] Shang, J. S., Chang, C. L., and Surzhikov, S. T., "Simulating Hypersonic Magnetofluid-Dynamic Compression in Rectangular Inlet," *AIAA Journal*, Vol. 45, No. 11, 2007, pp. 2710–2720. doi:10.2514/1.26086

[35] Shang, J. S., Menart, J., Kimmel, R., and Hayes, J., "Experimental Investigation of Magneto-Fluid-Dynamic Compression in a Cylindrical Inlet," AIAA Paper 2007-0399, Jan. 2007.

A. Ketsdever
Associate Editor